Electronic Supplementary Information

Programmable Mismatches-fueled High-efficiency DNA Signal Converter

Xiao-long Zhang, Zhe-han Yang, Yuan-yuan Chang, Di Liu, Yun-rui Li, Ya-qin Chai*, Ying Zhuo* and Ruo Yuan*

Key Laboratory of Luminescent and Real-Time Analytical Chemistry (Southwest University), Ministry of Education, School of Chemistry and Chemical Engineering, Southwest University, Chongqing 400715, PR China

* Corresponding author. Tel.: +86-23-68252277; Fax: +86-23-68253172.

E-mail address: yqchai@swu.edu.cn; yingzhuo@swu.edu.cn; yuanruo@swu.edu.cn

Table of contents

Experimental Section

Chemical and Materials. Gold chloride ($HAuCl_4 \cdot 4H_2O$), Tris (2-carboxyethy) phosphine hydrochloride (TCEP), and Hexanethiol (HT) were obtained from Sigma (St. Louis, MO, USA). The HPLC-purified oligonucleotides were purchased from Tsingke (Beijing, China) and Sangon Inc. (Shanghai, China), and Table S1 showed the oligonucleotides sequences used in the experiment. Tris-HCl buffer (20 mM Tris, 1.0 mM $MgCl_2$, 1.0 mM $CaCl_2$, 140 mM NaCl, 5 mM KCl, pH 7.4) was utilized to dilute oligonucleotides. 5xTBE buffer (250 mM Tris, 250 mM H_3BO_3, 10 mM EDTA, pH 8.0) was used to perform polyacrylamide gel electrophoresis (PAGE) experiments. Phosphate buffered solution (PBS) buffer (100 mM Na_2HPO_4, 100 mM KH_2PO_4, 100 mM KCl, pH 7.0) and $[Fe(CN)_6]^{3-/4-}$ solution (20 mM Tris-HCl, 5 mM $K_3[Fe(CN)_6]$, 5 mM $K_4[Fe(CN)_6]$, pH 7.4) were applied to accomplish the performance measurements of the electrochemical biosensor. TM buffer (10 mM Tris-HCl, 50 mM $MgCl_2$, 1 mM TCEP, pH 8.0) and TAE buffer (20 mM Tris-HCl, 20 mM CH_3COOH, 1 mM EDTA, 12.5 mM $Mg(OAc)_2$) were used to construct the DNA tetrahedrons nanoprobe (DTNP) and the triplex-forming oligonucleotide (TFO) separately.

Table S1. Synthetic Oligonucleotide Sequences

Primer name	Sequence (from 5' to 3')
A17	ATGATACAAAGAAAAGAAGCACATCGTTCGACATTACATC TTTTCTTTCTCTACA
B17	SH-$(CH_2)_6$-CATAACCTGGGACCGTAGATAATGTCGAACGATGTGACAC TTGACGGACCACTAT
C17	SH-$(CH_2)_6$-TCTTTTCTTTGTATCATGTAAGGGTGAAAGAAAAGAAAAT AGTGGTCCGTCAAGT

D17	SH-$(CH_2)_6$-TACGCTCCCAGGTTATGTTTCTTTTCTTTCACCCTTCGTGTAGAGAAAGAAAAGA
FS	AGAAAAGAAAAGGGTCAACATCAGTCTGATAAGCTA
TS	ATCAGACTGATGTTGACCCTTTTCTTTTCT
AP	ATCAGACTGATGTTGACCCTATATCCATAAATT
LS	TTTCTTTTCT-Fc
F1	ATGATACAAAGAAAAGA-6-FAM
F2	TCTTTTCTTTGTATCAT
F3	TTTCTTTTCT-BHQ1
miRNA-21	UAGCUUAUCAGACUGAUGUUGA
SM-miRNA-21	UAGAUUAUCAGACUGAUGUUGA
TM-miRNA-21	UAGAUUAUCAGACACAUGUUGA
miRNA-141	UAACACUGUCUGGUAAAGAUGG
miRNA-155	UUAAUGCUAAUCGUG AUAGGGGU
miRNA-182-5p	UUU GGC AAU GGU AGA ACU CAC ACU
let-7a	UGAGGUAGUAGGUUGUAUAGUU

Apparatus and Measurements. Cyclic Voltammetry (CV), Electrochemical Impedance Spectroscopy (EIS) and Square Wave Voltammetry (SWV) were carried out by employing a CHI760E electrochemical workstation (CH Instruments, Shanghai, China) with a three-electrode arrangement (with a platinum wire as the auxiliary, a saturated calomel electrode as the reference, and the modified glass carbon electrode (GCE) as the working electrode). Polyacrylamide Gel Electrophoresis (PAGE) was

accomplished by a Bio-Rad imaging system (Hercules, CA, USA). Ultraviolet-visible (UV-vis) spectra was performed by a UV-2501 PC Spectrometer (Shimadzu, Japan) and the fluorescence spectra was carried out with an F-2500 fluorescence spectrophotometer (Hitachi, Tokyo, Japan) with the slit width and the PMT voltage set as 5.0 nm and 700 V respectively. The atomic force microscope (AFM) was performed on the Dimension ICON (Bruker, America).The CV and EIS signal of the biosensor establishment were conducted in 2 mL 5 mM $[Fe(CN)_6]^{3-/4-}$ solution. CV was measured with a scanning potential from -0.2 V to 0.6 V (scan rate 100 mV/s). And the SWV was performed in 0.1 M PBS with the potential ranging from 0.2 V to 0.7 V (Amplitude 25 mV, Frequency 15 Hz, and Quiet time 2 s), which was harnessed to evaluate the electrochemical performance of the proposed biosensing platform under the optimal experimental conditions.

Preparation of DNA Tetrahedron Nanoprobe (DTNP). Equimolar quantities of four strands (A17, B17, C17, D17) were mixed in TM buffer (pH 8.0) at a final concentration of 1.0 μM and then heated to 95 °C for 10 min and cooled to 4 °C over 30 s for the formation of the DTNP. The prepared DTNPs were used in the subsequent experiments.

Assembly of the proposed Biosensing Platform. First, the bare glassy carbon electrode (GCE, 4 mm in diameter) was carefully polished with alumina slurry (0.3 μm and 0.05 μm) and sonicated with ethanol and deionized water. After that, the cleaned GCE was immersed into a $HAuCl_4$ aqueous solution (1%) and electrodeposited at −0.2 V for 30 s to obtain gold particles (depAu).

Subsequently, 10 μL of the DTNPs solution (1.0 μM) was dropped onto the electrode surface (depAu/GCE) and immobilized through Au−thiol interactions overnight at room temperature. After cleaning with TM buffer, the electrode was incubated with HT (1 mM) for 30 min to block the remaining active sites of electrode and then rinsed by ethanol and deionized water water for three times. Then the finished electrode (HT/DTNP/depAu/GCE) could be used for measurements.

Detection of Target miRNA based on the Enzyme-free Target Recycling Amplification (EFTRA). At first, the mixture of FS, AP and LS (3.0 μM) in TAE buffer (optimal pH) was heated to 95 ^{o}C for 10 min and then cooled down to room temperature for 60 min to form the three-strand DNA duplex (double helix). Then target miRNA-21 and TS (C) were added to the mixture above to react at 25 ^{o}C, from which the input target miRNA can convert into lots of output Fc-labeled product LS (B). At last, the DTNP-modified electrode was incubated with 10 μL of the reacted mixture to capture the LS (B) onto the electrode surface and then rinsed by the TAE buffer for subsequent experiments.

Cell Culture and Total RNA Extraction. The HeLa and MCF-7 cancer cells applied in this study were obtained from the cell bank of the Chinese Academy of Sciences (Shanghai, China). According to the manufacturer's instructions, the cancer cells were cultured in RPMI 1640 medium (Thermo Scientific Hyclone, USA) with the addition of 10% fetal calf serum (FCS), 100 U·mL^{-1} penicillin and 100 μg·mL^{-1} streptomycin at 37 °C in 5% CO_2 incubator. Then, the total RNA samples were extracted from the cancer cells by using the Trizol Reagent Kit (Sangon, Inc.,

Shanghai, China) on the basis of operating instructions. At last, the obtained cellular extracts were stored at −80 °C when not in use.

Polyacrylamide-Gel Electrophoresis (PAGE). Firstly, the DNA samples were mixed with the DNA-loading buffer (volume ratio 5:1), then the dynamic DNA-assembled products were analyzed by polyacrylamide-gel electrophoresis (PAGE) on a freshly prepared 16% or 8% polyacrylamide gel in 1× TBE buffer (pH 7.0 or 8.0) at 60 mA.

Characterization of the EFTRA, DTNP and TFO

The feasibility of EFTRA, DTNP and TFO was characterized by PAGE. As displayed in Fig. S1A, the bright bands in lanes 1−4 correspond to miRNA-21 (T), AP (A), TS (D), and FS (C) respectively, and lane 5 (without obvious band) corresponds to LS (B) which has only ten bases. Lane 6 corresponds to the three-stranded DNA Duplex ABC consisting of FS (C), AP (A) and LS (B). After the miRNA-21 (T) was mixed with Duplex ABC (lane 7), two additional bands with fast migration could be observed, suggesting the AP (A) (the bottom band in lane 7) was displaced and released accompanying with the forming of Duplex TBC (the middle band in lane 7). Then, after the TS (D) and miRNA-21 (T) were all mixed with the Duplex ABC (lane 8), the band corresponding to the Duplex ABC vanished, verifying the successful conversion from the Duplex ABC into Duplex TBC and Duplex DC (the most obvious bands in lane 8) through the EFTRA. These observations strongly indicated the EFTRA was successfully operated and the input of target miRNA-21 (T) could induce the output of the Fc-labeled LS (B) via it.

Then the PAGE analysis of DTNP was displayed in Fig. S1B. The obvious bands in lanes 1-4 correspond to the A17, B17, C17 and D17, respectively. After these four DNA strands were mixed to form DTNP by rapid solution annealing, only one obvious band with very low mobility corresponding DTNP could be noticed (lane 5), verifying the DTNP was successfully formed.

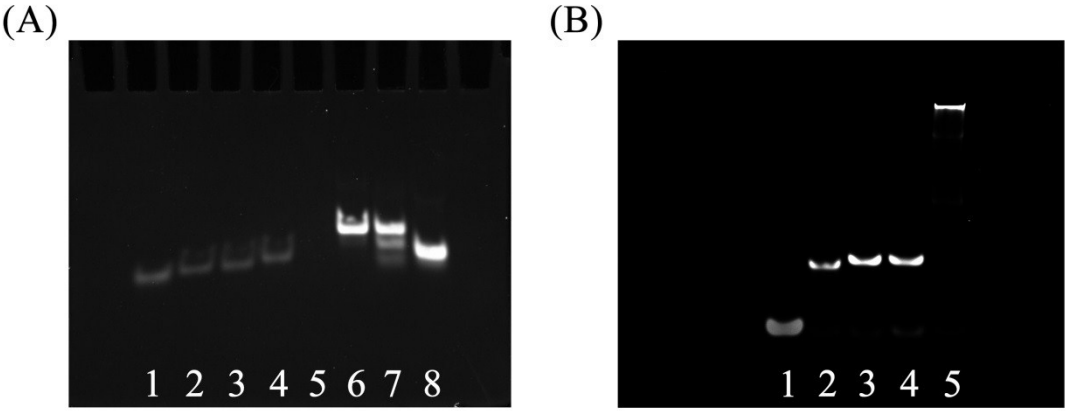

Fig. S1 Nondenaturing PAGE characterization of (A) EFTRA: lane 1, miRNA-21 (4 μM); lane 2, AP (A) (2 μM); lane 3, TS (D) (2 μM); lane 4, FS (C) (2 μM); lane 5, LS (B) (2 μM); lane 6, three-strand Duplex ABC (FS-AP-LS) (2 μM); lane 7, the mixture of miRNA-21 (2 μM) and Duplex ABC (2 μM); lane 8, the mixture of miRNA-21 (2 μM), TS (D) (2 μM), and Duplex ABC (2 μM) (PAGE 8%, 60 min), and (B) DTNP: lane 1, A17 (2 μM); lane 2, B17 (2 μM); lane 3, C17 (2 μM); lane 4, D17 (2 μM); lane 5, the mixture of A17 (2 μM), B17 (2 μM), C17 (2 μM), and D17 (2 μM) (PAGE 16%, 90 min).

And the TFO was characterized by both PAGE and UV-vis absorption spectra. As displayed in Fig. S2A (PAGE), lane 1 (without obvious band) and the obvious band in lane 2 correspond to Fc-labeled LS (B) and hairpin A17, separately. After the LS (B) was mixed with hairpin A17 for the TFO forming, an obvious band with slower migration comparing with the band in lane 2 could be observed (lane 3),

demonstrating the successful formation of TFO. Moreover, as the results of UV-vis absorption spectrum shown in Fig. S2B, curve a with an absorption maximum at 254 nm corresponding to the single strand LS (B), and curve b corresponding to the hairpin A17 with absorption position at 260 nm could be noticed and were consistent to the previous report,[1] which might be caused by the conjugated structure of DNA duplex. Then, after LS (B) was mixed with hairpin A17, in curve c, the absorption position at 260 nm shifted slightly towards longer wavelength regions (262 nm) and a distinctly enhanced spectral profile with an absorption maximum at 230 nm was observed, which might be the specific absorption position of TFO.[2,3] These results observed above confirmed that the TFO was successfully formed.

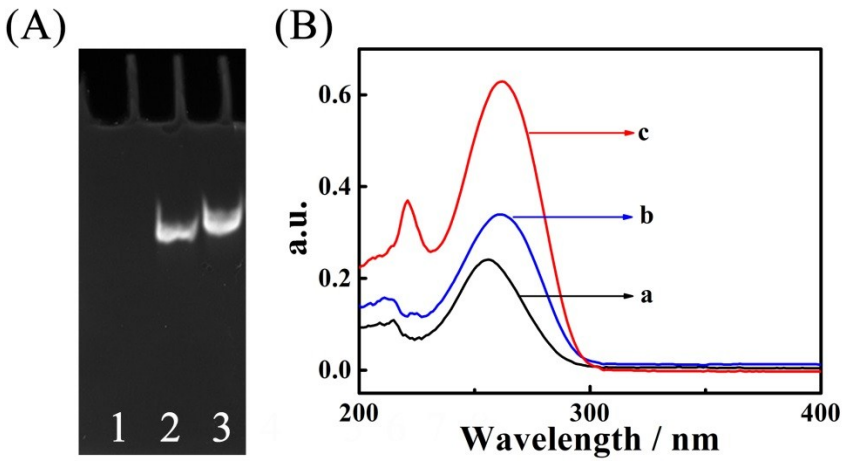

Fig. S2 (A) Nondenaturing PAGE characterization of TFO: lane 1, LS (2 μM); lane 2, hairpin A17 (2 μM); lane 3, LS (2 μM) and A17 (2 μM) (PAGE 16%，60 min). (B) UV-vis absorption spectra analysis of TFO: (a) LS (2 μM), (b) hairpin A17 (2 μM), (c) LS (2 μM) and hairpin A17 (2 μM).

Electrochemical Characterization of the Proposed Biosensing Platform

The CV and EIS were used to characterize the stepwise fabrication of the biosensing platform. As displayed in Fig. S3A (CV), a pair of well-defined redox

peaks (curve a) of the bare glass carbon electrode (GCE) could be noticed. When the GCE was electrodeposited with Au nanoparticles (depAu), the redox currents increased (curve b) resulting from the excellent conductivity of the AuNPs. Subsequently, with the immobilization of DTNPs, the redox currents decreased obviously (curve c) because of the repulsion effect between $[Fe(CN)_6]^{3-/4-}$ and the negatively charged DNA phosphate backbone. And when the HT was self-assembled on the electrode, the redox currents decreased slightly (curve c), further meaning that the electrode surface almost has been occupied with the DTNPs.

Then as illustrated in Fig. S3B (EIS), a small semicircle diameter and a long tail denoting diffusion could be observed owing to the well conductivity of the bare GCE (curve a). And we can find a nearly straight line after the depAu was modified onto the bare GCE (curve b) because of the large surface area and the excellent conductivity of the depAu. Next, with the self-assembly of more DNA strands and HT onto the electrode surface, a dramatical increasing trend of R_{et} (curves c, d) could be noticed, which was ascribed to the increased steric hindrance from the stack of DNA strands and HT. These EIS results were in accordance with the CV results observed above, further demonstrating the successful fabrication of this designed biosensing platform.

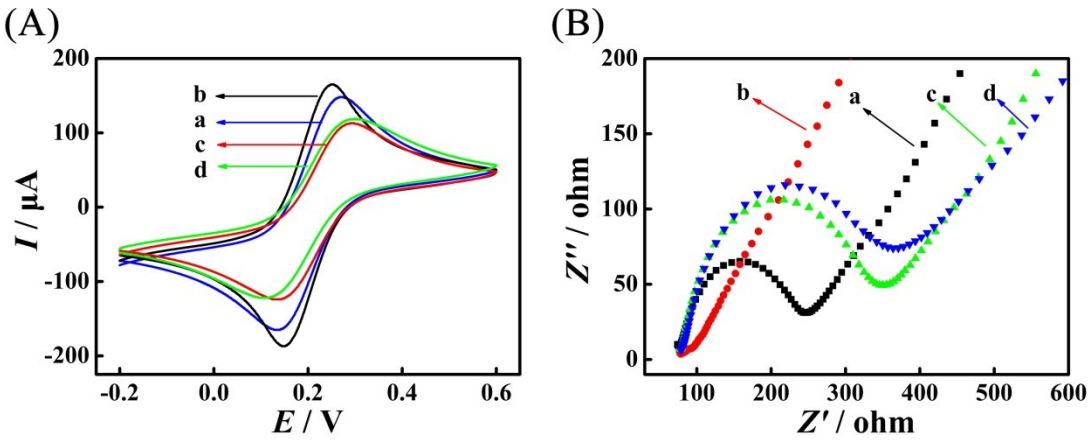

Fig. S3 (A) Typical CV responses and (B) EIS responses of different modified electrodes: (a) bare GCE, (b) depAu/GCE, (c) DTNP/depAu-GCE, (d) HT/DTNP/depAu/GCE.

Characterization of the Electrode Surface

We employ the atomic force microscope (AFM) to further verify the process happened on the electrode surface. As shown in Fig. S4, compared with the depAu (A), the height and the morphology of the DTNP/depAu (B) are slightly higher and more blurry at the edge of Au nanoparticles, respectively, sufficiently implying the DTNP was successfully modified on the depAu.

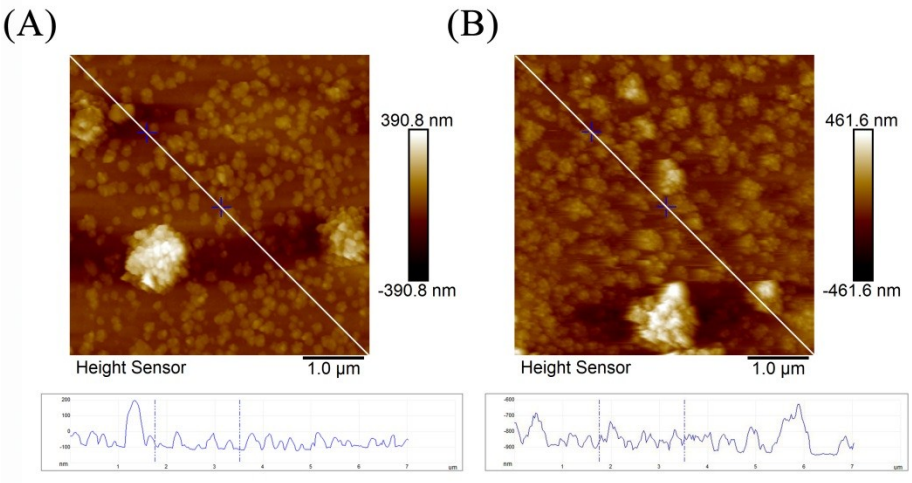

Fig. S4 AFM images of the modified films of: (A) depAu, (B) DTNP/depAu. Insets in the graph are corresponding height of sample on the diagonal.

Moreover, the electroactive area of the modified electrode (depAu/GCE) and the

density of DTNP on the modified electrode were also determined by cyclic voltammetry (CV) and chronocoulometry (CC). Firstly, CV studies were carried out according to the previous works[4, 5]. The cyclic voltammograms (CVs) were operated[1] at different potential scan rates (10, 30, 50, 70, 90, 110, 130, 150, 170, 190, and 210 mV/s) in 5 mM $Fe(CN)_6^{3-/4-}$ solution, as shown in following Fig. S5A. The linear regression for the peak current (I_p) *versus* the square root of scan rate ($v^{1/2}$) is presented in following Fig. S5B. According to the slope *S* and the Randles-Sevcik equation:

$$I_p = (2.69\times10^5)n^{3/2}AD^{1/2}Cv^{1/2} \qquad (1)$$

the electroactive area *A* can be expressed as eqn (2).

$$A = S/(2.69\times10^5)n^{3/2}D^{1/2}C \qquad (2)$$

where *n* is the number of electrons involved (n=1), *D* is the diffusion coefficient (6.72×10^{-6} cm^2 s^{-1}, 25 ℃), and *C* is the concentration of ferricyanide (5 mM). Thus the electroactive area *A* of the modified electrode was calculated as 21.5 mm^2.

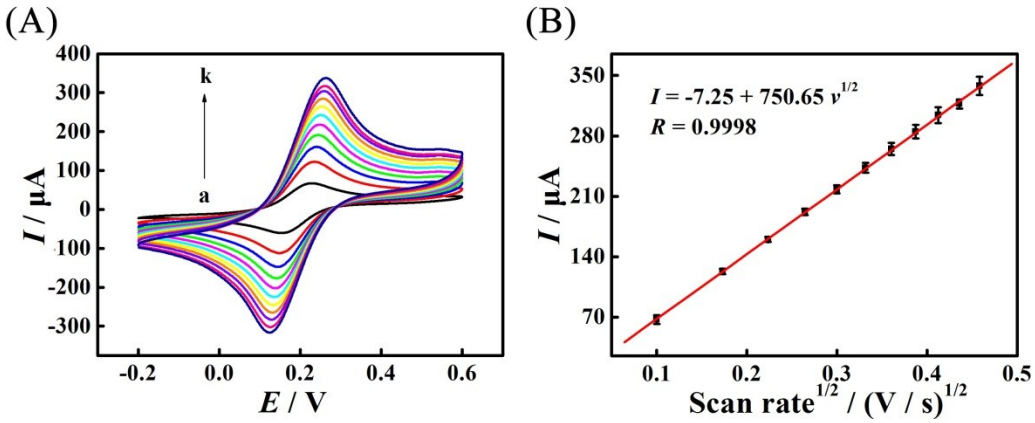

Fig. S5 (A) CVs of depAu/GCE in 5.0 mM $Fe(CN)_6^{3-/4-}$ at different scan rates (a-k: 10, 30, 50, 70, 90, 110, 130, 150, 170, 190, and 210 mV/s); (B) Calibration curve for I_p *vs* $v^{1/2}$.

Secondly, according to the previous report[6], the CC studies were performed and

the density of DTNP Γ_{ss} was calculated by using the following eqn (3) and (4).

$$\Gamma_{ss} = (Q_{ss}N_A/nFA)(z/m) \qquad (3)$$

$$Q_{ss} = Q_{total} - Q_{dl} \qquad (4)$$

And N_A is Avogadro's number, n is the number of electrons, A is the electroactive area, m is the number of nucleotides in the DNA and z is the charge of the redox molecule. Q_{total} and Q_{dl} are obtained from the plot of the charge (Q) versus the square root of scan time ($t^{1/2}$), as shown in following Fig. S6. So the density of DTNP on depAu/GCE in this work is 5.5×10^{11} molecules cm^{-2}.

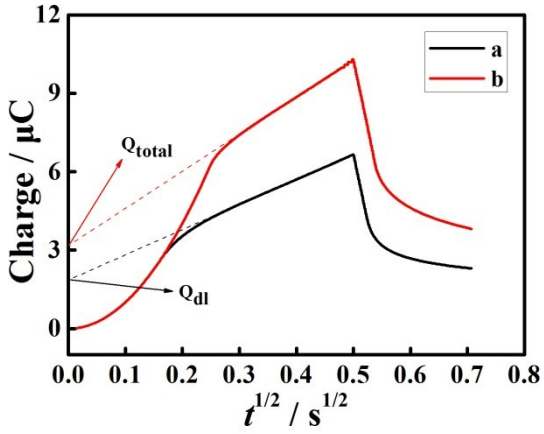

Fig. S6 Chronocoulometric curves of depAu/GCE modified with DTNP (a) in 10 mM Tris-HCl (pH 7.4) and (b) in 10 mM Tris-HCl (pH 7.4) containing 50 μM RuHex.

Optimization of Experimental Conditions

Because the accuracy and the sensitivity of this proposed biosensing platform largely depend on the efficiency of the EFTRA and the formation of TFO, four experimental parameters including the reaction time, pH of TFO forming and additional pH of TFO unwinding, and the reaction time of the EFTRA were optimized. Firstly, as shown in Fig. S7A, with the increase of the reaction time of the TFO

forming, the current response increased and reached a maximum after 90 min because of the reaction equilibrium, therefore the reaction time of the formation of TFO was fixed at 90 min. Moreover, as shown in Fig. S7B, the current response slightly increased with the pH of TAE buffer increased from 5.5 to 7.0 and reached the maximum at pH = 7.0, showing the optimal pH for TFO was 7.0. And with the pH of TAE buffer changed from 8.5 to 10.5 after TFO was formed, the current response decreased obviously and reached a plateau after the pH = 10.0 (Fig. S7C), confirming that overly alkaline TAE buffer could promote the TFO dissociation and the optimal pH for this process was 10.0, thus the optimal pH of TAE buffer for regeneration of the DTNP was fixed at 10.0. Then the effect of the EFTRA reaction time was also studied by SWV. The current response increased with the increase of the reaction time and reached a plateau after 120 min, suggesting the reaction equilibrium after 120 min (Fig. S7D). As a result, the optimal reaction times of TFO forming and EFTRA were fixed at 90 min and 120 min separately, and 7.0 and 10.0 were chosen the optimal pH of TAE buffer for the TFO forming and unwinding respectively.

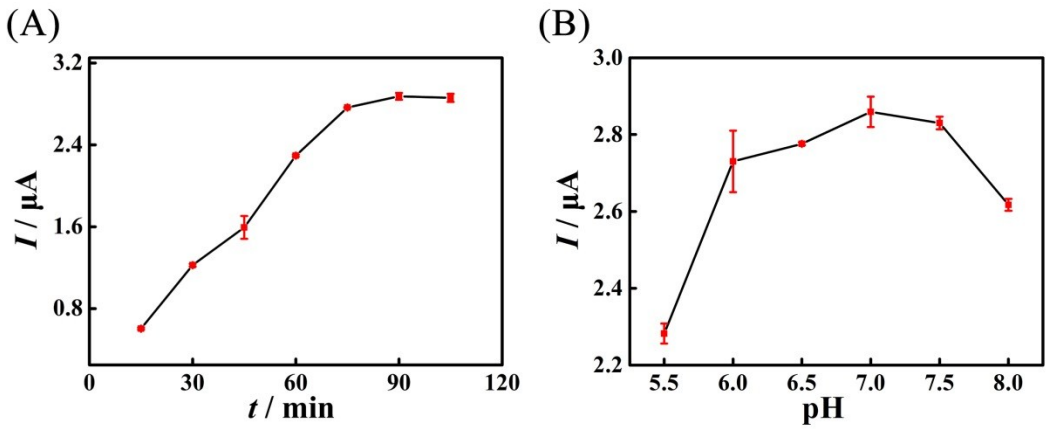

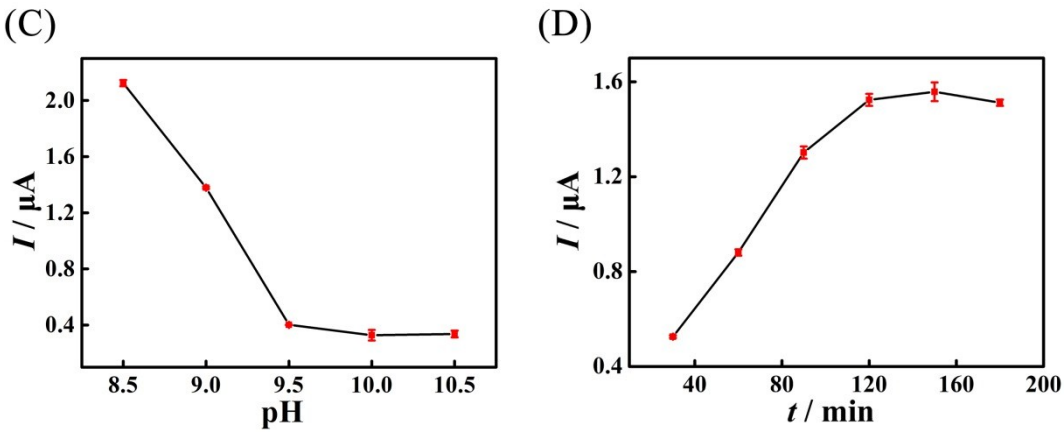

Fig. S7 Effect on the current response of the proposed biosensing platform with different experimental parameters: (A) the reaction time of the TFO forming (15 min, 30 min, 45 min, 60 min, 75 min, 90 min, with DTNP concentration of 1 μM and LS concentration of 3.5 μM and reaction temperature of 25 °C, TAE buffer 7.0); (B) the pH of TAE buffer for TFO forming (5.5, 6.0, 6.5, 7.0, 7.5, 8.0); (C) the pH of TAE buffer for TFO unwinding (8.5, 9.0, 9.5, 10.0, 10.5); (D) the reaction time of the EFTRA (30 min, 60 min, 90 min, 120 min, 150 min, 180 min, with miRNA-21 concentration of 1 nM and reaction temperature of 25 °C)

The Binding Affinity (K_a) of TFO

We have also measured the binding affinity of TFO according to Scatchard analysis[7,8] using fluorescence spectra. Specially, the mixture of FAM-labeled F1 and F2 (2.0 μM) in TAE buffer (optimal pH) was heated to 95 °C for 10 min and then cooled down to room temperature for 60 min to form the DNA Duplex F1F2. After that, the BHQ1-labeled F3 with various concentrations was applied to form TFO with Duplex F1F2 and determine the fluorescence intensity of it. As displayed in Fig. S8A, the fluorescence intensity (with excitation wavelength and emission wavelength of 496 nm and 529 nm respectively) decreased as the concentration of F3 elevated from 0 μM to 2.66 μM further showing the successful formation of TFO. Moreover we

simulated the formation of TFO using a one-step reaction model for measuring the K_a:

F1F2 + F3 = F1F2F3

Where the DNA Duplex F1F2 are fluorescent and the TFO F1F2F3 are non-fluorescent. Then based on the Fig. S8B, the equilibrium concentrations of all DNA species can then be derived by solving a set of equations:

$$[\text{F1F2F3}] = (1 - a) \times c \qquad (5)$$

$$[\text{F1F2}] = a \times c \qquad (6)$$

$$[\text{F3}] = a \times c \qquad (7)$$

Where a and c represent the dissociation degree of TFO and the concentration of F1F2F3 without any dissociation at point A (Fig. S8B) respectively. And $a = F'/F$, where F' and F represent the fluorescence intensity of point B and initial DNA Duplex F1F2 (Fig. S8B) separately. Thus the dissociation constant K_d can be obtained by the equation:

$$K_d = \frac{[\text{F3}] \times [\text{F1F2}]}{[\text{F1F2F3}]} = \frac{a^2 \times c}{(1 - a)} = \frac{(F'/F)^2 \times c}{(1 - F'/F)} \qquad (8)$$

Then based on the equation (8), the K_d of TFO was ultimately obtained with the value of 6.4×10^{-8} M which was similar to the previous report,[9] and the affinity constant K_a can be estimated as 1.56×10^{7} M^{-1}.

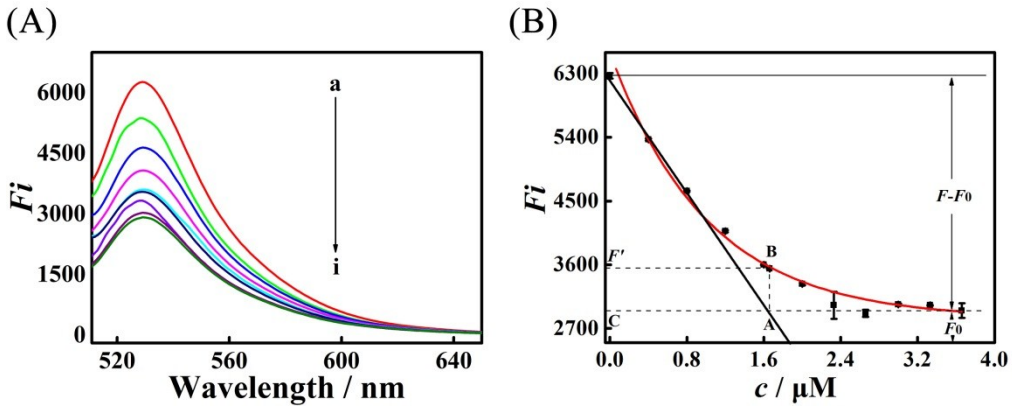

Fig. S8 (A) The variation of fluorescence intensity of the solution (containing DNA Duplex F1F2) with different concentrations of F3 (a) 0 μM, (b) 0.4 μM, (c) 0.8 μM, (d) 1.2 μM, (e) 1.6 μM, (f) 1.66 μM, (g) 2.0 μM, (h) 2.33, (i) 2.66 μM. (B) Relationship between the fluorescence intensity and the F3 concentration.

The SWV Responses of the Electrochemical Biosensing Platform under Different Conditions

Besides, we investigated the stepwise fabrication of DTNP-modified biosensing electrode with SWV to verify the feasibility of this platform for responding to the Fc-labeled LS (B). As displayed in Fig. S9A, compared with the blank signal response (curve a), an obvious current response arose with the incubation of Fc-labeled LS (B) on the prepared biosensing platform (curve b), indicating that LS (B) were successfully captured onto the electrode surface by DTNP through forming the TFO. Moreover, even with the presence of other interfering DNAs containing TS (D), Duplex ABC (FS-AP-LS) and Duplex DC (TS-FS), the current responses (curve c, d) hardly changed comparing with curve b, further suggesting that this prepared biosensing platform could be utilized to accurately detect the quantified independent Fc-labeled LS (B) and the output Fc-labeled LS (B) from the input target via EFTRA

respectively. And as displayed in Fig. S9B, the prepared biosensing platform showed a relatively low SWV intensity without the presence of target miRNA (curve a). However, when the biosensing surface was modified with reacted solutions after the EFTRA was triggered by target, the SWV signal increased significantly (curve b), demonstrating this biosensing platform is qualified for further detecting target miRNA based on the EFTRA.

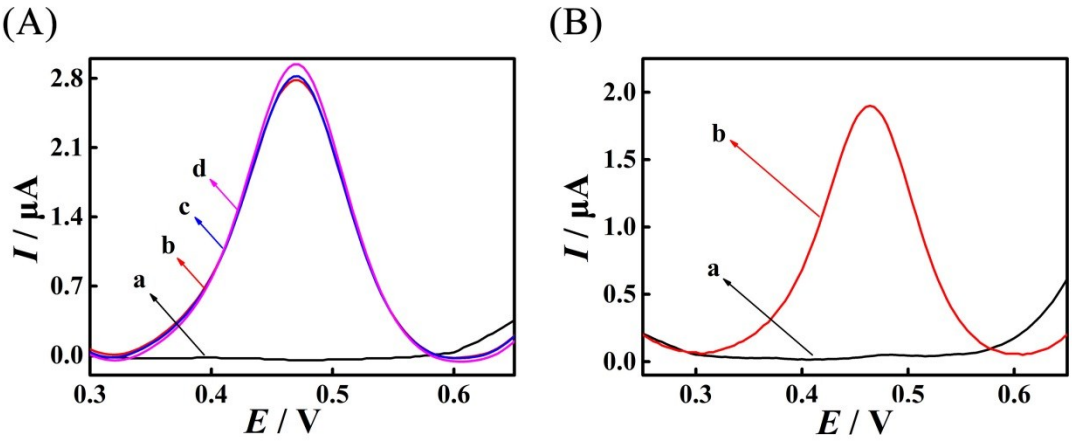

Fig. S9 SWV response of the prepared biosensing platform: (A) (a) with blank sample; (b) with LS (3.0 μM); (c) with LS (3.0 μM) and TS (3.0 μM); (d) with LS (3.0 μM), TS (3.0 μM), Duplex FS-AP-LS (3.0 μM) and Duplex FS-TS (3.0 μM), and (B) (a) without and (b) with target miRNA (100 nM).

Measure of Experimental Conversion Efficiency of EFTRA (*N*)

To obtain the experimental conversion efficiency of EFTRA (*N*), we firstly carried out the relationship of the current response of biosensor and the concentration of the quantified independent Fc-labeled LS (B) based on the SWV, under the optimal conditions, as shown in Scheme 1, the biosensing platform was directly incubated with different concentrations of LS (B), which can be captured by the prepared DTNP through forming the TFO and cause an amplified current response on the electrode

surface (Part B). As shown in Fig. S10A, the SWV current response increased as the concentration of LS (B) from 0.1 nM to 3.5 μM and displayed a fine linear relationship with the concentration (0.1 μM - 3.5 μM (1×10^{-7} M - 3.5×10^{-6} M)) and the logarithm concentration (0.1 nM – 0.1μM (1×10^{-10} M - 1×10^{-7} M)) of the LS (B) respectively (Fig. S10B, S10C). The corresponding regression equation was I = 0.1613 lg c + 1.8217 (from 0.1 nM to 0.1μM (1×10^{-10} M - 1×10^{-7} M), R=0.9991) and I = 0.7406 c + 0.6262 (from 0.1 μM to 3.5 μM (1×10^{-7} M - 3.5×10^{-6} M), R=0.9994) separately (I and c represented the SWV current response and LS (B) concentration, separately; unit of c was M).

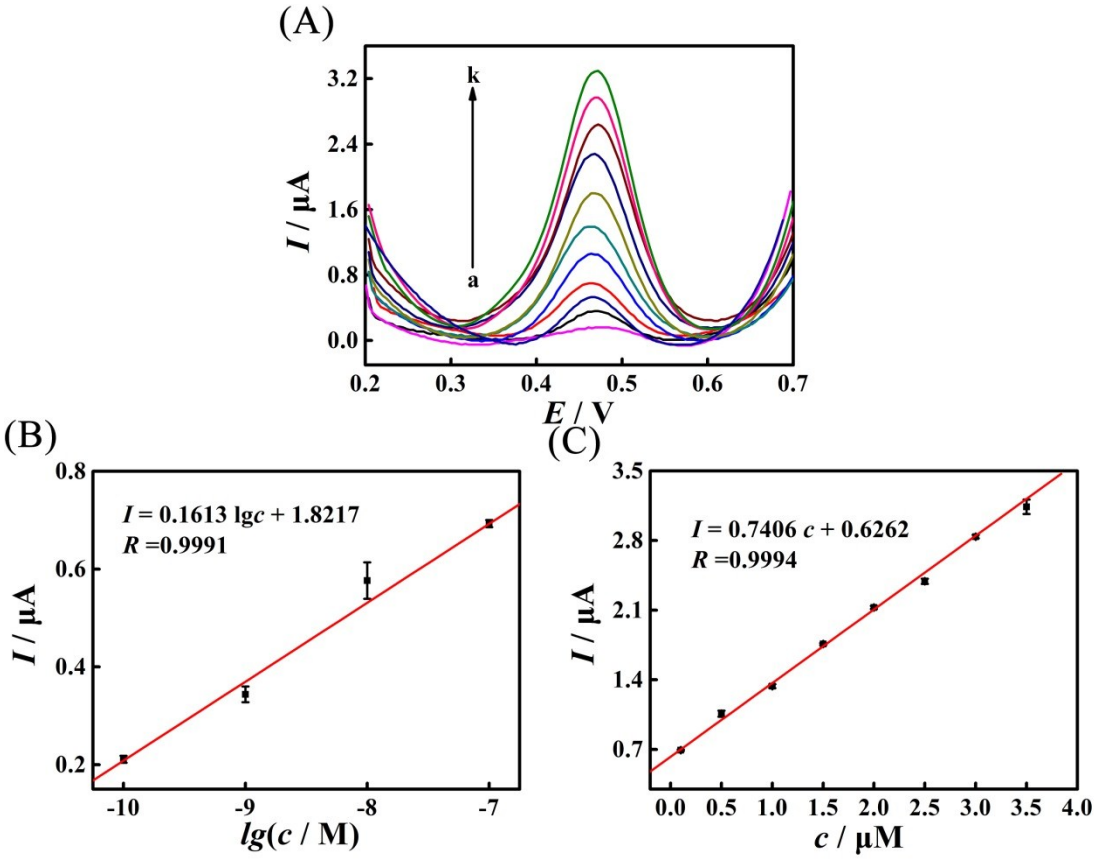

Fig. S10 (A) SWV current responses of the proposed biosensing platform to different concentrations of the quantified independent Fc-labeled LS (B): (a) 0.1 nM, (b) 1.0 nM, (c) 10 nM,

(d) 100 nM, (e) 0.5 μM, (f) 1.0 μM, (g) 1.5 μM, (h) 2.0 μM, (i) 2.5 μM, (j) 3.0 μM, (j) 3.5 μM. Corresponding calibration plot for the SWV current value *vs* (B) lg *c* (from 0.1 nM to 100 nM) and (C) *c* (from 100nM to 3.5 μM) respectively.

Moreover, under the optimal conditions (Fig. S11), we measured SWV current responses of the proposed biosensing platform to different concentrations of miRNA-21 based on the EFTRA. As shown in Fig. S11A, via the wild-type EFTRA, the current response gradually increased with the concentration of target increased from 10 fM to 100 nM (1×10^{-14} M - 1×10^{-12} M) and displayed a well linear relationship with the logarithm of the miRNA-21 concentration. And as illustrated in Fig. S11B, the regression equation is expressed as $I = 0.2480 \lg c + 3.7297$ (I is the SWV peak current, and c is the concentration of target miRNA-21,) with a correlation-coefficient value (R) of 0.9984. According to the 3σ rule, a detection limit of 1.22 fM for miRNA-21 was calculated out (Table S6).

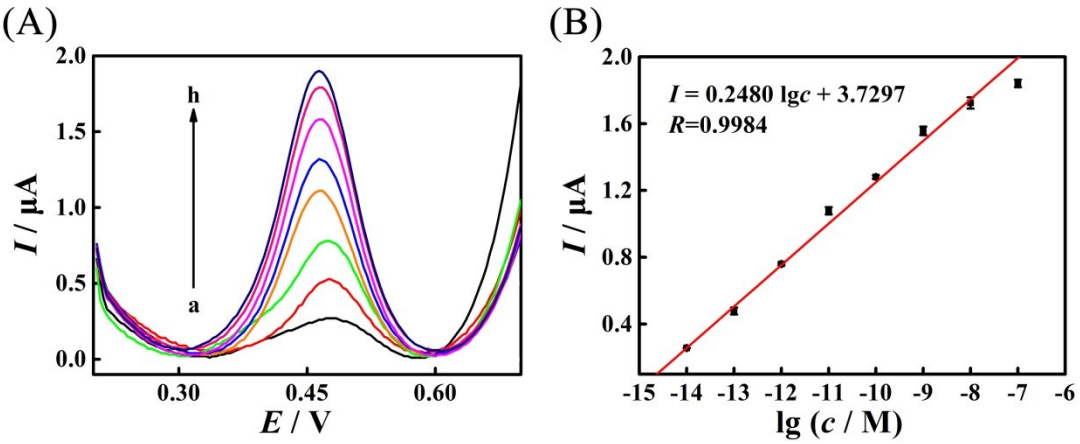

Fig. S11 (A) SWV current responses of the biosensing platform to different concentrations of the target miRNA-21: (a) 10 fM, (b) 100 fM, (c) 1.0 pM, (d) 10 pM, (e) 100 pM, (f) 1.0 nM, (g) 10 nM, (h) 100 nM, and (B) the calibration plot for the SWV peak current vs lg *c* (*c* represents the miRNA-21 concentration).

Then based on the regression equation of current response to the concentration of LS (B) and target miRNA respectively, the experimental conversion efficiency of EFTRA (*N*) was obtained (Table S2).

Computation of the Theoretical Conversion Efficiency of EFTRA (*N′*)

To compute the theoretical conversion efficiency of EFTRA (*N′*), we introduced three tunable variables c_1, c_2, and c_3 and two dependent variables x and y in the equations (where A, B, C, D, T separately represents the AP, LS, FS, TS, and target miRNA, and c_1= $[T]_0$, c_2= $[ABC]_0$, c_3= $[D]_0$, x= [A] and y= [TBC]).

$$K_1 = e^{\frac{-\Delta G_1}{RT}} = \frac{[A] \times [TBC]}{[T] \times [ABC]} = \frac{x \times y}{(c_1 - y) \times (c_2 - x)} \quad (9)$$

$$K_2 = e^{\frac{-\Delta G_2}{RT}} = \frac{[T] \times [B] \times [DC]}{[D] \times [TBC]} = \frac{(c_1 - y) \times (x - y)^2}{(c_3 - x + y) \times y} \quad (10)$$

Then by solving this two equations (9) and (10) (T = 25 °C, R = 1.987 × 10^{-3} kcal. K^{-1}. mol^{-1}, c_2 and c_3 were fixed at 3 μM, ΔG_1 and ΔG_2 were calculated using NUPACK software,[10] K_1 and K_2 were obtained by the equations), we calculated out ratio of the balanced concentration of output Fc-labeled LS ([B] = x-y) and initial concentration of target miRNA ($[T]_0$ = c_1), which represents the theoretical EFTRA conversion efficiency (*N′*) ((x-y)/ c_1). And the results of theoretical *N′* of wild-type EFTRA were shown in Table S2.

Theoretical and Experimental Conversion Efficiency of Wild-type EFTRA with Different Concentration of Target

Table S2. Theoretical and Experimental Conversion Efficiency of Wild-type

EFTRA with Different Concentration of Target (T = 25 °C, $c_2 = c_3$ = 3 μM, ΔG_1 = -0.2 kcal·mol^{-1}, ΔG_2=-0.36 kcal·mol^{-1}, K_1= 1.40, K_2 = 1.84)

c_1	N'	N
10 fM	299676617.31	19841.80
100 fM	29967661.73	47330.33
1 pM	2996766.17	179989.20
10 pM	299676.62	61004.59
100 pM	29967.66	8854.98
1 nM	2996.77	1256.82
10 nM	299.68	148.23
100 nM	29.97	16.40

Mismatched Sequences

Table S3. Mismatched Sequences

Primer name	Sequence (5' to 3')
AP-D1M1t	ATC AGA tTG ATG TTG ACC CTA TAT CCA TAA ATT
AP-D1M1a	ATC AGA aTG ATG TTG ACC CTA TAT CCA TAA ATT
AP-D1M1g	ATC AGA gTG ATG TTG ACC CTA TAT CCA TAA ATT
AP-D2M1c	ATC AGA CTG cTG TTG ACC CTA TAT CCA TAA ATT
AP-D2M1g	ATC AGA CTG gTG TTG ACC CTA TAT CCA TAA ATT
AP-D2M1t	ATC AGA CTG tTG TTG ACC CTA TAT CCA TAA ATT
AP-D3M1c	ATC AGA CTG ATG cTG ACC CTA TAT CCA TAA ATT

AP-D3M1a	ATC AGA CTG ATG aTG ACC CTA TAT CCA TAA ATT
AP-D3M1g	ATC AGA CTG ATG gTG ACC CTA TAT CCA TAA ATT
AP-D4M1c	ATC AGA CTG ATG TTG cCC CTA TAT CCA TAA ATT
AP-D4M1g	ATC AGA CTG ATG TTG gCC CTA TAT CCA TAA ATT
AP-D4M1t	ATC AGA CTG ATG TTG tCC CTA TAT CCA TAA ATT
AP-D1D4M2	ATC AGA tTG ATG TTG cCC CTA TAT CCA TAA ATT
AP-D2D4M2	ATC AGA CTG cTG TTG cCC CTA TAT CCA TAA ATT
AP-D3D4M2	ATC AGA CTG ATG cTG cCC CTA TAT CCA TAA ATT
AP-D1D3D4M3	ATC AGA tTG ATG cTG cCC CTA TAT CCA TAA ATT
AP-D2D3D4M3	ATC AGA CTG cTG cTG cCC CTA TAT CCA TAA ATT
AP-D1D2D3D4M4	ATC AGA tTG cTG cTG cCC CTA TAT CCA TAA ATT

Thermodynamic Parameters, Theoretical and Experimental Conversion Efficiency of EFTRA with Different Mismatches

Table S4. Thermodynamic Parameters, Theoretical and Experimental Efficiency of EFTRA with Different Mismatches (T = 25 °C, $c_2 = c_3 = 3$ μM, ΔG_2=-0.36 kcal·mol^{-1}, K_2 = 1.84)

Sequence	ΔG_1 (kcal.mol^{-1})	K_1	N'	N
AP	-0.2	1.40	2996766.17	179989.20
AP-D1M1t	-4.13	1065.67	2999882.52	263300.03
AP-D1M1a	-3.55	400.35	2999808.36	236970.02
AP-D1M1g	-2.94	142.97	2999679.34	199972.99

AP-D2M1c	-4.23	1261.62	2999892.02	270051.31
AP-D2M1g	-3.07	178.06	2999712.66	228193.36
AP-D2M1t	-3.80	610.53	2999844.80	246826.90
AP-D3M1c	-4.54	2129.05	2999916.87	289765.26
AP-D3M1a	-3.86	675.60	2999852.46	251417.77
AP-D3M1g	-2.81	114.80	2999642.17	192816.64
AP-D4M1c	-5.31	7810.11	2999956.56	309343.78
AP-D4M1g	-2.94	142.97	2999679.34	203078.58
AP-D4M1t	-4.18	1159.51	2999887.37	261274.64
AP-D1D4M2	-9.24	5938315.19	2999998.03	420334.87
AP-D2D4M2	-9.34	7030258.41	2999998.15	445314.61
AP-D3D4M2	-9.64	11665286.78	2999998.44	473129.89
AP-D1D3D4M3	-13.58	9020536010.00	2999999.15	1051579.80
AP-D2D3D4M3	-13.67	10500490442.00	2999999.15	1189305.97
AP-D1D2D3D4M4	-17.61	8119821995495.69	2999999.15	2050769.65

Theoretical and Experimental Conversion Efficiency of Evolved EFTRA with Different Concentration of Target.

Table S5. Theoretical and Experimental Conversion Efficiency of Evolved HEEFTRA with Different Concentration of Target (T = 25 °C, $c_2 = c_3 = 3$ μM, ΔG_1 = -9.64 kcal·mol^{-1}, ΔG_2=-0.36 kcal·mol^{-1}, K_1= 11665286.78, K_2 = 1.84)

c_1	N'	N
10 fM	299999887.30	55377.76

100 fM	29999988.36	379354.52
1.0 pM	2999998.44	473129.89
10 pM	299999.49	75182.28
100 pM	29999.80	12419.66
1.0 nM	2999.93	1779.37
10 nM	299.98	192.92
100 nM	29.99	23.53

Calculation of Detection Limit for the miRNA Biosensing

On the basis of IUPAC definition, we have calculated the limit of detection according to equation (11), the calibration plot ((12), without mismatches introduction) and ((13), with mismatches introduction) where x_B is the SWV intensity of blank sample, s_B is the standard deviation of blank samples and I_L is the current of detection limit, and IUPAC suggests that $k = 3$ allows a confidence level of 99.86%.[11]

$$I_L = x_B + k \times s_B \quad (11)$$

$$I = 0.2480 \lg c + 3.7297 \quad (12)$$

$$I = 0.2657 \lg c + 4.1775 \quad (13)$$

In this paper, specifically, the SWV measurements for blank samples were executed with ten parallel tests and the results were shown in Table S6.

Table S6. Limit of Detection Calculation for the miRNA Biosensing

Biosensor	x_B	s_B	Detection limit
Without mismatches	1.60E-08	5.06E-09	1.22 fM

With mismatches	1.67E-08	5.68E-09	0.25 fM

Reproducibility, Specificity, and Stability of the Proposed Biosensor

In order to further study the performance of this proposed biosensor with mismatches comprehensively, the reproducibility, specificity and stability of the biosensing platform were validated. To confirm the reproducibility of the biosensor, the necessary index for a real biomarker detection, four prepared biosensors with 1 nM miRNA-21 were studied under the same determination condition. As displayed in Fig. S12A, a relative standard deviation (RSD) of 5.79% was achieved. Moreover, a set of electrodes with same miRNA-21 (1 nM) were detected after 10 days, and the RSD is 4.43%. The remarkable results indicate that the combination of the evolved HEEFTRA and DTNP for biomarker detection presented a desirable reproducibility.

To assess the specificity of this biosensor, four interference agents including miroRNA-141 (miRNA-141), microRNA-155 (miRNA-155), microRNA-182-5P (miRNA-182-5P) and let-7a were evaluated under the same experimental condition. As shown in Fig. S12B, the obvious current response of the electrode could be observed only with miRNA-21. Oppositely, in the presence of the interference agents including miRNA-141 (1 nM), miRNA-155 (1 nM), miRNA-182-5p (1 nM) and let-7a (1 nM), the current responses were negligible. Besides, the mixed analytical solution containing 10 pM of target miRNA-21 was also analyzed with the biosensing system, exhibiting an obvious current response as expected. Moreover, we choose single-mismatched miRNA-21 (SM-miRNA-21) and triple-mismatched miRNA-21

(TM-miRNA-21) to further verify the specificity of the proposed biosensing platform. As shown in Fig. S9C, in the presence of SM-miRNA-21 or TM-miRNA-21 with 10-fold concentration (100 pM), the current responses are all unobvious comparing with the one of target miRNA-21 (10 pM), further indicating that the developed biosensor is sensitive to the mutation happened in the target miRNA-21. These results above demonstrated the high specificity of the biosensor.

The stability, which was critical to its practical application especially in a complicated biomedical environment, was evaluated by successive scans of the sensing platform with detection of 3.5 μM strands LS for 20 times. As displayed in Fig. S12D, when compared with the initial electrochemical response, the SWV current intensity only changed from 97.3% to 103.4% with the RSD=1.79%, indicating an excellent stability of our proposed biosensor.

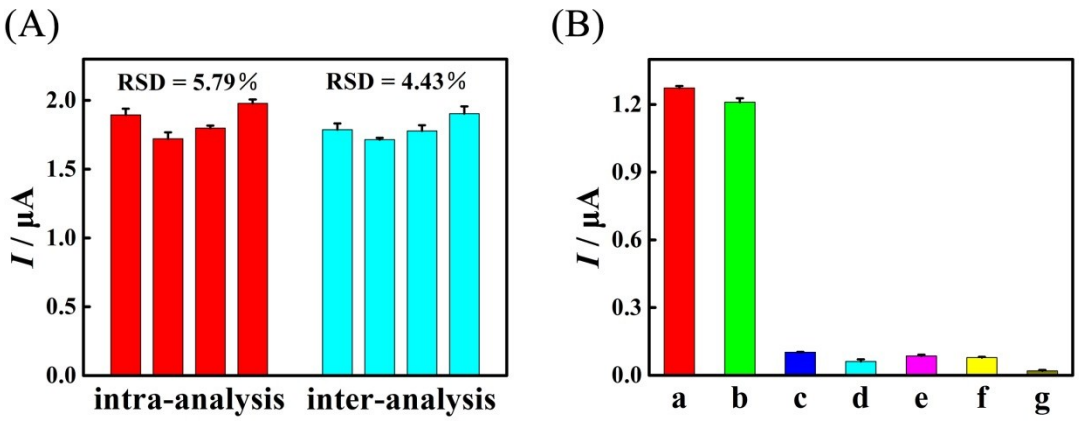

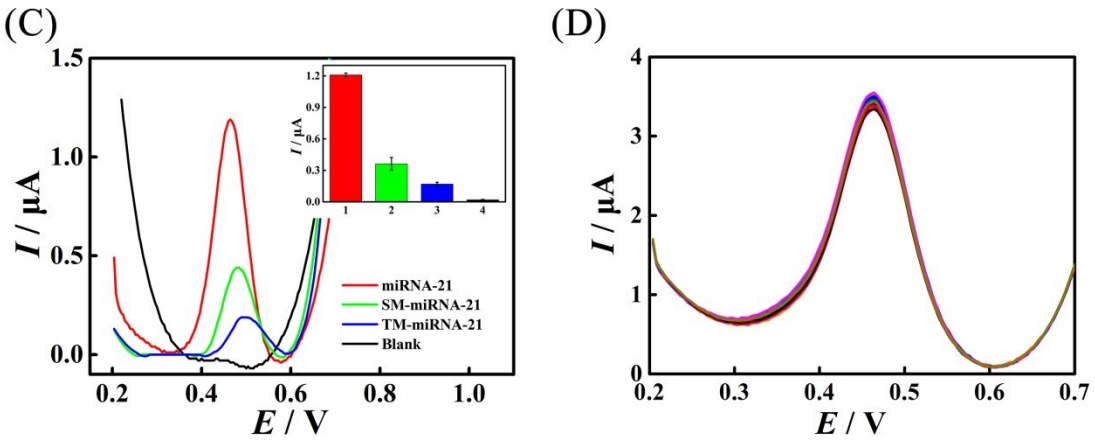

Fig. S12 (A) Reproducibility of the elaborated miRNA biosensing system (1 nM miRNA-21). (B) Specificity of the electrochemical biosensor: (a) miRNA-21 (10 pM), (b) mixed sample containing (a), (c), (d), (e), and (f), (c) miRNA-141 (1 nM), (d) miRNA-155 (1 nM), (e) miRNA-182-5P (1 nM), (f) let-7a (1 nM), and (g) blank sample. (C) SWV response for complementary target (10 pM), SM strand (100 pM), TM strand (100 pM), and blank sample. Inset in part C, the corresponding peak currents. (D) Stability of the proposed biosensor (3.5 μM LS (B)).

Real Application of the Developed Biosensor in Cancer Cells

The capacity of the developed biosensor for determination of miRNA-21 in real biological samples was studied by taking the total RNA extraction solutions from the human cancer cell lines (MCF-7 and HeLa). As shown in Fig. S13, the SWV response gradually increased as the cell numbers increased, exhibiting a significant expression level of target miRNA-21 from MCF-7, however, in blank sample and HeLa cells, no obvious SWV responses were noticed, suggesting a relatively low expression level compared to MCF-7. The above results were consistent to previous research,[12-14] further suggesting this quantification of miRNA-21 in cancer cells possesses the key potential for clinical diagnosis of cancers.

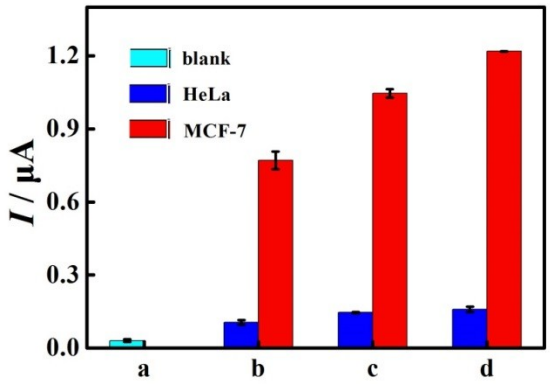

Fig. S13 Data analysis of the prepared biosensor from different cancer-cell lysates: (a) blank sample, (b) HeLa (100 cells) and MCF-7 (100 cells), (c) HeLa (1000 cells) and MCF-7 (1000 cells), and (d) HeLa (10000 cells) and MCF-7 (10000 cells).

The Reversible pH-switching of the Developed Biosensing Platform

Actually, under the optimal pH, we also studied the reversibility of the proposed biosensing platform. When incubated with the blank TAE buffer (pH= 10.0), the DTNP could be regenerated by the dissociation of the TFO on the electrode surface at such pH. As displayed in Fig. S14A, after the TFO was formed at pH=7.0, an obvious SWV response (curve b) could be observed in comparison with the initial blank current response of the independent DTNPs (curve a). However, after immersing in the TAE buffer at pH=10.0, the current response of the electrode (curve c) decreased about 90% comparing with curve b and reversed to be unobvious and similar to the initial one (curve a), demonstrating the successful regeneration of the biosensor. Significantly, the reversible prepared biosensing platform was assessed for seven times, with a regeneration-rate range from 89.01% to 90.56% (Fig. S14B), which further implied the good reversible pH-switching of the biosensor and suggested that the biosensing platform could potentially be reused for many times.

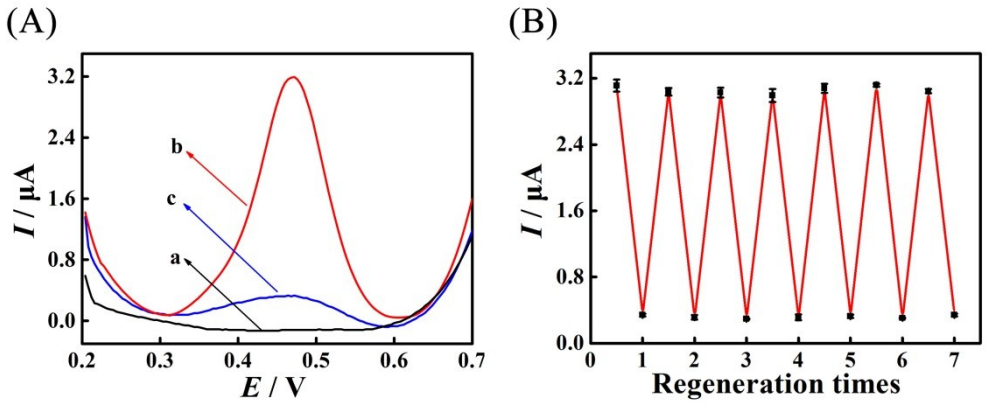

Fig. S14 (A) SWV current responses of the prepared biosensing platform (a) before and (b) after the TFO formation and of (c) one regeneration of the biosensing platform. (B) Regeneration of the biosensing platform (seven times) under the same conditions.

REFERENCES

1 S. Kundu, H. Liang, *Adv. Mater*., 2008, **20**, 826-831.

2 X. Liang, H. Asanuma, M. Komiyama, *J. Am. Chem. Soc.*, 2002, **124**, 1877-1883.

3 Y. Hu, A. Cecconello, A. Idili, F. Ricci, I. Willner, *Angew. Chem. Int. Ed.*, 2017, **56**, 15210-15233.

4 F. X. Wang, C. Ye, S. Mo, H. Q. Luo, J. R. Chen, Y. Shi and N. B. Li, *Anal. Bional. Chem.*, 2019, **411**, 3059-3068.

5 J. Singh, A. Roychoudhury, M. Srivastava, P. R. Solanki, D. W. Lee, S. H. Lee and B. D. Malhotra, *Nanoscale*, 2014, **6**, 1195-1208.

6 J. Zhang, S. Song, L. Wang, D. Pan and C. Fan, *Nat. Protoc.*, 2007, **2**, 2888-2895.

7 J. Sap, A. Munoz, K. Damm, Y. Goldberg, J. Ghysdael, A. Leutz, H. Beug, B. Vennstrom, *Nature*, **1986**, 324, 635-640.

8 J. J. Siekierka, S. H. Y. Hung, M. Poe, C. S. Lin, N. H. Sigal, *Nature*, 1989, **341**, 755-757.

9 A. Patterson, F. Caprio, A. Vallée-Bélisle, D. Moscone, K. W. Plaxco, G. Palleschi, F. Ricci, *Anal. Chem*., 2010, **82**, 9109-9115.

10 R. M. Dirks, J. S. Bois, J. M. Schaeffer, E. Winfree, N. A. Pierce, *SIAM Rev.*, 2007, **49**, 65-88.

11 A. Radi, J. L. Acero Sánchez, E. Baldrich, C. K. O'Sullivan, *J. Am. Chem. Soc.*, 2006, **128**, 117-124.

12 Z. Wang, J. Han, Y. Cui, X. Zhou, K. Fan, *Biochem. Biophys. Res. Commun.*, 2013, **439**, 384-389.

13 J. Lu, A. Tsourkas, *Nucleic Acids Res.*, 2009, **37**, e100.

14 S. Li, L. Xu, W. Ma, X. Wu, M. Sun, H. Kuang, L. Wang, N. A. Kotov, C. Xu, *J. Am. Chem. Soc*., 2016, **138**, 306-312.